

# A method of moments based CFD model for polydisperse aerosol flows with strong interphase mass and heat transfer

David P. Brown <sup>a,b,\*</sup>, Esko I. Kauppinen <sup>b</sup>, Jorma K. Jokiniemi <sup>c</sup>,  
Stanley G. Rubin <sup>d</sup>, Pratim Biswas <sup>e</sup>

<sup>a</sup> *StreamWise, 5860 Leeland St. S., St. Petersburg, FL 33715, United States*

<sup>b</sup> *Helsinki University of Technology, Center for New Materials, Biologinkuja 7, Espoo, P.O. Box 1602, FIN-02044 VTT, Finland*

<sup>c</sup> *VTT Processes, Small Particle Group, Biologinkuja 7, Espoo, P.O. Box 1602, FIN-02044 VTT, Finland*

<sup>d</sup> *Digital Simulation Laboratory, Department of Aerospace Engineering and Engineering Mechanics, University of Cincinnati, Cincinnati, OH 45221-0070, United States*

<sup>e</sup> *Environmental Engineering Science, Cupples II, Room 208, One Brookings Drive, Campus Box 1180, Washington University in St. Louis, St. Louis, MO 63130-4899, United States*

Available online 22 March 2006

---

## Abstract

A Computational Fluid Dynamics method is introduced to study the nucleation, coagulation, evaporation and condensation of polydisperse particles in multi-dimensional multi-species laminar and turbulent flows with strong mass and energy coupling between the phases. The model is based on the Reduced Navier–Stokes (RNS) methodology and incorporates a lognormal aerosol moment method to describe the evolution of suspended particulates. The model is validated against available analytic and numerical techniques for one and two-dimensional geometries. The sensitivity of both the bulk flow and aerosol particle properties to boundary layer effects, even in high Reynolds number flows, is demonstrated for transonic two-phase flow in wet steam de Laval nozzles. It is shown that the developed model and method are useful for the prediction of particle properties such as mass and number concentrations, geometric mean particle size and standard deviation of the particle size distribution in multi-dimensional turbulent compressible aerosol flows with strong heat and mass transfer.

© 2006 Elsevier Ltd. All rights reserved.

---

## 1. Introduction

Understanding and predicting polydisperse aerosol behavior is critical to the development of many advanced technologies related to combustion, pollution prediction and control, fouling, powder and materials manufacture and even to the administration of drugs and purification of silicon chips. In many of these systems, the bulk fluid behavior and that of the suspended particulates can become strongly coupled due to mass, momentum and energy transfer between the aerosol vapor and condensed phases. Understanding such multi-phase processes requires

detailed knowledge of complex fluid behavior coupled with transport and dynamics of gas species and liquid and solid particulates. Aerosol parameters such as size, polydispersity, concentration, composition and morphology are a function of residence time in critical regions of the flow, local thermodynamic conditions such as temperature and pressure (and hence saturation conditions), as well as mixing efficiencies and chemical reactions affecting heat, mass and momentum transfer. These are in turn functions of factors such as entrainment of surrounding fluid due to viscosity and large and small scale structures in the flow such as vorticity, recirculation and turbulence. In many of these circumstances, the coupling between the gas phase and suspended aerosol particles can become significant and neglecting such effects can lead to erroneous predictions of overall system behavior.

---

\* Corresponding author. Address: StreamWise, 5860 Leeland St. S., St. Petersburg, FL 33715, United States.

## Nomenclature

$a$	speed of sound of mixture ( $\sqrt{\gamma RT_f^*}$ ) (m/s)	$Kn$	Knudsen Number ( $\lambda^*/r_g^*$ ) (ND)
$A_1$	first coefficient of Stokes number ( $= \frac{2\rho_p^* U_\infty}{9\mu_f^* L_\infty} C_{Tg}^{*2}$ ) (ND)	$K_T$	thermophoretic constant ( $=0.55$ ) (ND)
$A_2$	second coefficient of Stokes number ( $= \frac{\rho_p^* U_\infty}{9\mu_f^* L_\infty} 3.314 \lambda^* r_g^*$ ) (ND)	$L$	length (m)
$A_3$	first coefficient of Schmidt number ( $= \frac{\rho_f^* k_B T_f^*}{6\mu_f^* r_g^*} C$ ) (ND)	$m$	mass (kg)
$A_4$	second coefficient of Schmidt number ( $= \frac{\rho_f^* k_B T_f^*}{12\mu_f^* r_g^*} 3.314 \lambda^*$ ) (ND)	$M$	Mach number of mixture $\sqrt{\frac{u_f^{*2} + v_f^{*2} + w_f^{*2}}{\gamma RT_f^*}}$ (ND)
$A_{1,2}^+$	Baldwin–Barth Constants ( $=26, 10$ ) (ND)	$M_k$	$k$ th volume moment of the distribution ( $m^{3k}/m^3$ )
$b_0$	(Ref. [29]) $0.633 + .092\sigma^2 - .022\sigma^3$ (ND)	$MW$	mixture molecular weight (Ref. [11]) ( $\sum_{s=1}^{N_s} \rho_s C_s + \rho_a C_a$ ) / $\sum_{s=1}^{N_s} \frac{\rho_s C_s}{MW_s}$ (kg/mol)
$b_1$	(Ref. [29]) $0.39 + .5\sigma - .214\sigma^2 + .029\sigma^3$ (ND)	$n(v)$	particle number concentration ( $\#/m^3$ )
$B_1$	$(36\pi)^{1/3} v_1^* n^* \sqrt{k_B T_f^* / (2\pi m_1^*)}$ (m/s)	$N_s$	number of gas phase species (ND)
$B_2$	$\sqrt{6k_B T_f^* r_g^* / \rho_p^*}$ ( $m^3/s$ )	$P$	pressure ( $kg/m\ s^2$ )
$B_3$	$\frac{1}{3} \left( (48\pi^2)^{1/3} \lambda^* v_1^* n_s \sqrt{8k_B T_f^* / \pi m_1^*} \right)$ ( $m^2/s$ )	$Pe$	Peclet number ( $ReSc$ ) (ND)
$B_4$	$2k_B T_f^* / (3\mu_f^*)$ ( $m^3/s$ )	$Pr$	Prandtl Number ( $C_p \mu_f / k$ ) (ND)
$C_c$	Cunningham correction factor (ND)	$q$	heat flux ( $kg/s^3$ )
	$C(v_p) = 1 + 1.257 \lambda^* v_g^{*-1/3} \left( \frac{3}{4\pi} \right)^{1/3}$ (Ref. [45])	$R$	universal gas constant ( $kg\ m^2/s^2\ Kmol$ )
$C_a$	mass fraction of condensed phase (ND)	$Re$	combined Reynolds number ( $Re_l + Re_t$ ) (ND)
$C_p$	mixture specific heat at constant pressure (Ref. [4]) $\sum_{s=1}^{N_s} C_s C_{ps} + C_a C_{pa}$ (J/kg K)	$Re_l$	laminar Reynolds number ( $\rho_\infty U_\infty L_\infty / \mu_{l\infty}$ ) (ND)
$C_s$	mass fraction of species $s$ (ND)	$Re_t$	turbulent Reynolds number ( $\rho_\infty U_\infty L_\infty / (\mu_f^*)$ ) (ND)
$c_{e1,2}$	Baldwin–Barth Constants ( $=1.2, 2.0$ ) (ND)	$s$	surface area ( $m^2$ )
$c_\mu$	Baldwin–Barth Constant ( $=0.09$ ) (ND)	$S$	saturation ratio (ND)
$d$	diameter (m)	$Sc$	Schmidt number ( $Sc = \frac{\mu_f^*}{\rho_f^* D_p} = \frac{\mu_f^* 18 m_p^2}{\rho_p^* k_B T_f^* d_p^2 C}$ ) (ND)
$D$	diffusion Coefficient ( $k_B T_f^* \tau^* / m^*$ ) ( $m^2/s$ )		$Sc_0 = 1 / (A_3 v_g^{-1/3} \exp(0.5 \ln^2 \sigma) + A_4 v_g^{-2/3} \exp(2 \ln^2 \sigma))$
$D_{1,2}$	1st and 2nd turbulent dissipation coefficients (ND)		$Sc_1 = 1 / (A_3 v_g^{-1/3} \exp(-2.5 \ln^2 \sigma) + A_4 v_g^{-2/3} \exp(-4 \ln^2 \sigma))$
$E_t$	total energy ( $m^2/s^2$ )		$Sc_2 = 1 / (A_3 v_g^{-1/3} \exp(5.5 \ln^2 \sigma) + A_4 v_g^{-2/3} \exp(-10 \ln^2 \sigma))$
$f_2$	dissipation function (Ref. [52]) (ND)	$St$	Stokes number ( $St = \frac{\tau^* U_\infty}{L_\infty} = \frac{\rho_p^* U_\infty}{18 \mu_f^* L_\infty} C_c d_p^{*2}$ ) (ND)
	$\frac{c_{e1}}{c_{e2}} + \left( 1 - \frac{c_{e1}}{c_{e2}} \right) \left( \frac{1}{\kappa y^+} + D_1 D_2 \right)$ $\times \left( \sqrt{D_1 D_2} + \frac{y^+}{\sqrt{D_1 D_2}} \exp(A_1^+ / y^+) D_2 \right)$ $+ \frac{y^+}{\sqrt{D_1 D_2}} \exp(A_2^+ / y^+) D_1$		$St_0 = A_1 v_g^{2/3} \exp(2 \ln^2 \sigma) + A_2 v_g^{1/3} \exp(0.5 \ln^2 \sigma)$ $St_1 = A_1 v_g^{2/3} \exp(8 \ln^2 \sigma) + A_2 v_g^{1/3} \exp(3.5 \ln^2 \sigma)$ $St_2 = A_1 v_g^{2/3} \exp(14 \ln^2 \sigma) + A_2 v_g^{1/3} \exp(6.5 \ln^2 \sigma)$
$g$	Jacobian of the coordinate transformation (ND)	$T$	mixture temperature (K)
$G$	condensation rate ( $m^3/m^3\ s$ )	$u, v, w$	Cartesian components of velocity (m/s)
$H_t$	total enthalpy ( $m^2/s^2$ )	$U, V, W$	contravariant components of velocity (ND)
$HV$	heat of vaporization ( $m^2/s^2$ )	$U$	velocity vector (ND)
$HR$	heat of reaction ( $m^2/s^2$ )	$v$	volume ( $m^3$ )
$I$	nucleation rate ( $\#/m^3\ s$ )	$W_k$	transformed aerosol moment ( $W_k = \ln(M_k / (\rho + 1))$ ) (ND)
$k^0$	critical number of monomers in a cluster (ND)	$x, y, z$	Cartesian coordinates in physical space (m)
$k_B$	Boltzman's constant ( $kg\ m^2/s^2\ K$ )	$Y$	Species mole fraction (ND)
$K$	adjustable constant (ND)	$\alpha_k$	$k$ th condensation coefficient (ND)
		$\beta$	collision frequency function ( $\#/m^3\ s$ )

$\gamma$	mixture ratio of specific heats ( $1 - R/MWC_p$ ) (ND)	<i>Subscripts</i>	
$\gamma_k$	$k$ th coagulation coefficient (ND)	a	aerosol phase
$\delta$	boundary layer thickness (m)	$j$	$\xi, \eta, \zeta$
$\Delta$	change due to aerosol formation and growth (ND)	Con	due to condensation
$\varepsilon_k$	Lennard-Jones Temperature (K)	C	convective
$\kappa$	thermal conductivity ( $\text{kg/s}^3 \text{ K}$ )	D	diffusional
$\eta$	collection Efficiency (ND)	f	bulk fluid
$\lambda$	mean free path of gas mixture ( $\lambda^* = \frac{\mu_f^*}{\rho_f^*} \sqrt{\frac{\pi m_f^*}{2 k_B T_f^*}}$ ) (m)	g	geometric mean
$\phi$	Knudsen correction ( $\frac{2\lambda + d_p}{d_p + 5.33(\lambda^2/d_p) + 3.42\lambda}$ ) (ND)	I	inertial
$\Phi$	energy dissipation function ( $\text{kg/m s}$ )	$k$	$k$ th aerosol moment
$\mu$	viscosity ( $\text{kg/m s}$ )	l	laminar
$\rho$	mixture density $\sum_{s=1}^{N_s} \rho_s + \rho_a$ ( $\text{kg/m}^3$ )	L	local
$\sigma$	standard deviation of aerosol size distribution, Lennard-Jones Diameter (ND, Å)	Nuc	due to nucleation
$\Sigma$	dimensionless nucleation group ( $\frac{\sigma v_1^3}{k_B T_f^*}$ ), surface tension (ND, N/m)	p	particle
$\tau$	viscous stress tensor, characteristic time ( $\tau = \frac{\rho_p d_p^2 C_c}{18 \mu_f^*}$ ) ( $\text{kg/m s}^2$ , s)	Rxn	due to chemical reaction
$\xi, \eta, \zeta$	Transformed coordinates in computational space (ND)	$s$	gas phase species $s$
$\varpi$	vorticity (m/s)	t	turbulent, total
$\varpi = \sqrt{\left(\frac{\partial u_f}{\partial y} - \frac{\partial v_f}{\partial x}\right)^2 + \left(\frac{\partial v_f}{\partial z} - \frac{\partial w_f}{\partial y}\right)^2 + \left(\frac{\partial w_f}{\partial x} - \frac{\partial u_f}{\partial z}\right)^2}$		T	thermophoretic
$\wp$	turbulent Production ( $\text{kg/m s}^3$ )	v	viscous
		w	wall value
		$\Sigma$	surface tension
		$\xi, \eta, \zeta$	differentiated with respect to $\xi, \eta, \zeta$
		1	monomer
		32	Sauder mean
		$\infty$	initial, free stream or characteristic value
		<i>Superscripts</i>	
		*	dimensional quantity
		0	critical value
		$i$	$x, y, z$
		c	continuum
		fm	free molecular
		$k$	to the power $k$

The computation of such complex processes can be carried out using a variety of numerical techniques but has typically been approached by solving the flow in an Eulerian reference frame and tracking particles through the flow field in a Lagrangian reference frame. In such schemes, aggregate aerosol properties are computed by summing contributions of discrete particle sizes and composition from the complete size distribution within a given flow or by integrating particle properties along streamlines. However, in order to accurately account for the particle behavior (e.g. agglomeration, nucleation, and growth) and thus its influence on the bulk fluid, the population balance equation (PBE) [1–3] should be solved together with the continuity equation, momentum balance equations and the energy balance equation. To date, attempts to incorporate the PBE into computational fluid dynamics (CFD) codes have been limited. A logical extension of the Eulerian–Lagrangian approach is the Monte-Carlo simulation technique in which the solution of the PBE is formulated in terms of its stochastic equivalent [4,5]. Here,

a representative population of particles evolves according to an appropriate balance of probabilities. However, due to the large number of particles that need to be tracked in order to provide a statistically reasonable representation of the physics, the computational expense is still too large for the formulation to be implemented in practical applications.

Significant reductions in computational effort can be achieved using an Eulerian formulation for multi-phase processes [6] and, in recent years, several researchers have tried to couple the PBE via Euler representations of the dispersed phase. In general, these can be classified as monodisperse methods, discrete population balance (DPB) or sectional methods and moment methods. In monodisperse methods, details of the PBE are neglected and only the overall volume fraction of the dispersed phase is accounted for [7–9]. In the DPB technique [10], the continuous particle size distribution is represented as a collection of discrete particle size bins each representing a range of particle properties and with appropriate transport and dynamics terms

applied for each size class. There have been numerous models developed for one-dimensional flows using such techniques e.g. [11–18]. In order to achieve reasonably accurate resolution and to overcome numerical diffusion, however, the particle size distribution must be divided into a large number of bins. Consequently, implementation in CFD codes becomes prohibitive for all but the most restrictive cases [19–26].

An alternative approach is the methods of moments (MOM) in which the moments of the particle size distribution are solved by integrating out the internal coordinate (e.g. diameter or volume). This allows the problem to be reconstructed in a reduced variable space and in which each moment is a transportable scalar, however, the problem of mathematical closure arises [27,28]. Three methods are typically employed to resolve the closure issue: through the assumption of a closed form of the distribution function in which the properties of the distribution are a function of the solved moments [29–31], though complex closure rules based on interpolation between moments [28] or through quadrature methods [32]. Depending on the method of closure, the number of unknowns can be reduced to as few as three, which makes implementation into CFD codes tractable [33–39]. However, to date, many issues related to interphase coupling have been ignored. In particular, the combined effects of mass and heat transfer with the evolution of the polydisperse aerosol size distribution has received no attention in the literature.

Our previous work has modeled polydisperse aerosol transport in two and three-dimensions as well as the effects of chemical reaction and gas phase species mixing on the evolution of the aerosol size distribution [40–42]. The present work describes a method of computing aerosol systems with strongly coupled heat and mass transfer and extends many aspects of previous research into a comprehensive model of coupled fluid/species/aerosol behavior which can be applied to a wide range of problems. This method uses an Eulerian moment form of the general dynamic equation for aerosol behavior developed using a lognormal size distribution in conjunction with a Reduced Navier–Stokes (RNS) formulation [43] for bulk fluid modeling which allows large time steps and rapid convergence. It is demonstrated that this RNS/moment model is effective in solving for behavior of polydisperse aerosols in general laminar/turbulent, incompressible/transonic/supersonic, flows with strong coupling between the bulk flow, individual gas phase species and suspended particles. Many important parameters, such as spatial/temporal distributions of aerosol properties and depositional efficiencies, can be calculated directly without having to sum up results for monodisperse aerosols over the entire particle spectrum or without having to solve for a large number of unknowns. This formulation can significantly reduce computational effort as compared with schemes based on Lagrangian or Eulerian sectional representations of aerosol behavior.

## 2. Governing equations and boundary conditions

Four sets of governing equations are considered here: those related to the transport of mass, momentum and energy in bulk fluid flow, those related to the conservation of individual species in the fluid, those related to the production, dissipation and transport of turbulence, and those related to the transport and dynamics of suspended particles within the fluid flow. These sets of equations can be strongly coupled to each other and must be solved simultaneously in many instances, though, in the low particle concentration limit, the coupling between the fluid dynamics and particle dynamics is one-way. Details of the derivations of the governing equations can be found in [40–42].

### 2.1. Bulk fluid equations

The bulk fluid flow is described by the compressible Reduced Navier–Stokes (RNS) [43] equations. They are derived using a perturbation expansion for large Reynolds number: omitting higher order streamwise diffusion terms in the full Navier–Stokes equations. The formulation reduces to the Euler equations when all viscous diffusion and heat transfer terms are neglected. This results in a composite system of the full Euler and higher order boundary layer equations. The RNS equations can thus be used to solve both the inviscid and viscous regions simultaneously, providing an efficient way of solving both internal and external flow fields at a lower computational cost than many full Navier–Stokes (FNS) solvers. Other advantages of the RNS method include simplified consistent boundary conditions, sharp shock capturing without the use of explicit artificial viscosity, and faster convergence than time-dependent Navier–Stokes solvers. The Full Navier–Stokes solution can be recovered by replacing the remaining diffusion terms in a deferred-corrector (DC) [44].

The RNS method has been verified extensively over a wide range of conditions including 1-D/2-D/3-D, incompressible/hypersonic, viscous/inviscid, laminar/turbulent, steady/unsteady and internal/external flows. The present code is written in conserved variable form and incorporates velocity flux splitting for continuity and convective terms. Using the following non-dimensionalization,

$$\begin{aligned} x &= \frac{x^*}{L}, & y &= \frac{y^*}{L_\infty}, & z &= \frac{z^*}{L_\infty} \\ u_f &= \frac{u_f^*}{U_{f\infty}}, & v_f &= \frac{v_f^*}{U_{f\infty}}, & w_f &= \frac{w_f^*}{U_{f\infty}} \\ \rho_f &= \frac{\rho_f^*}{\rho_{f\infty}}, & \mu_f &= \frac{\mu_f^*}{\mu_{f\infty}}, & P_f &= \frac{P_f^*}{\rho_{f\infty} U_{f\infty}^2} \end{aligned} \quad (1)$$

the RNS equations with source terms due to fluid/aerosol particle coupling and with multiple species in the gas phase can be written in vector form as

$$\begin{aligned}
& \text{diag}\left(1, 1, 1, 1, \frac{1}{\rho_f}\right) \frac{\partial}{\partial \tau} \left[ \sqrt{g} \begin{pmatrix} \rho \\ \rho u_f \\ \rho v_f \\ \rho w_f \\ H_t - (\gamma - 1)M^2 P \end{pmatrix} \right] \\
& + \frac{\partial}{\partial \xi} \left[ \sqrt{g} \begin{pmatrix} \rho U_f \\ \rho U_f u_f + \xi_x p \\ \rho U_f v_f + \xi_y p \\ \rho U_f w_f + \xi_z p \\ U_f H_t \end{pmatrix} \right] + \frac{\partial}{\partial \eta} \left[ \sqrt{g} \begin{pmatrix} \rho V_f \\ \rho V_f u_f + \eta_x p - \tau_x^\eta \\ \rho V_f v_f + \eta_y p - \tau_y^\eta \\ \rho V_f w_f + \eta_z p - \tau_z^\eta \\ V_f H_t - \Phi_\eta + q_\eta \end{pmatrix} \right] \\
& + \frac{\partial}{\partial \zeta} \left[ \sqrt{g} \begin{pmatrix} \rho W_f \\ \rho W_f u_f + \zeta_x p - \tau_x^\zeta \\ \rho W_f v_f + \zeta_y p - \tau_y^\zeta \\ \rho W_f w_f + \zeta_z p - \tau_z^\zeta \\ W_f H_t - \Phi_\zeta + q_\zeta \end{pmatrix} \right] = \begin{bmatrix} \Delta m \\ 0 \\ 0 \\ 0 \\ \Delta H_t \end{bmatrix} \quad (2)
\end{aligned}$$

where  $\rho$  is the mixture density where  $(\rho = \rho_f + \rho'_a)$  and  $(\rho_f = \sum_{s=1}^{N_s} \rho_s)$ ;  $\text{diag}$  is a diagonal matrix;  $U_f$ ,  $V_f$  and  $W_f$  are contravariant velocities.  $u_f$ ,  $v_f$  and  $w_f$  are Cartesian velocities where

$$u_f = x_\xi U_f + x_\eta V_f + x_\zeta W_f \quad (3)$$

$$v_f = y_\xi U_f + y_\eta V_f + y_\zeta W_f$$

$$w_f = z_\xi U_f + z_\eta V_f + z_\zeta W_f$$

$H_t$  is the total enthalpy.  $\Delta H_t$  and  $\Delta m$  are the heat and mass addition due to aerosol formation and growth,  $q_j$  the heat flux. Sources due to momentum transfer and buoyancy are not considered here.  $x$ ,  $y$  and  $z$  are Cartesian coordinates.  $\xi$ ,  $\eta$  and  $\zeta$  are transformed coordinates.  $g$  is the inverse Jacobian of the coordinate transformation.  $\tau_i^j$ ,  $\Phi_j$  represent the RNS approximated viscous stress tensor and viscous energy dissipation respectively. Subscripts connote the derivative of the subscripted quantity with respect to the subscripted variable.  $\gamma$  is the ratio of specific heats of the aerosol and  $M$  is the Mach number for the mixture defined from the relations [11]

$$C_p = \sum_{s=1}^{N_s} C_s C_{p_s} + C_a C_{p_a} \quad (4)$$

$$\text{MW} = \left( \sum_{s=1}^{N_s} \rho_s C_s + \rho_a C_a \right) / \sum_{s=1}^{N_s} \frac{\rho_s C_s}{\text{MW}_s} \quad (5)$$

$$\gamma = (1 - R/\text{MW} C_p) \quad (6)$$

$$M = \sqrt{\frac{u^{*2} + v^{*2} + w^{*2}}{\gamma R T^*}} \quad (7)$$

where  $N_s$  is the number of gas phase species,  $C_p$  is the specific heat at constant pressure and  $\text{MW}$  is the molecular weight for the mixture, including the condensed phase.  $\rho_a$  and  $C_{p_a}$  are calculated based on mass concentration of aerosol per unit gas volume. Note that equivalent molecular weight for the aerosol,  $\text{MW}_{a,s}$  is neglected in the  $\text{MW}$  calculation since it appears in the denominator of a summation and is much larger than the gas phase molecular weights.

Closure of the equations is achieved with the equation of state

$$\gamma_\infty M_\infty^2 \frac{C_p}{R} P = \rho \left( H_t - \frac{1}{2} (\gamma_\infty - 1) M_\infty^2 (u^2 + v^2 + w^2) \right) \quad (8)$$

## 2.2. Aerosol equations

The present method uses an Eulerian moment form of the general dynamic equation (GDE) developed assuming a lognormal size distribution [29,45] which has been found to exist in a wide range of aerosol systems [46]. The model incorporates contributions for particle transport (due to convection, diffusion, thermophoresis and inertia) and dynamics (due to coagulation, nucleation, evaporation and condensation).

### 2.2.1. Aerosol transport

The aerosol conservation equation can be written as

$$\frac{\partial n_p(v_p)}{\partial t} + \nabla \cdot (n_p(v_p) \mathbf{U}_p) = 0 \quad (9)$$

where  $n_p(v_p)$  is the dimensionless particle size distribution function,  $\mathbf{U}_p$  is the dimensionless particle velocity vector.  $\mathbf{U}_p$  can be defined as  $\mathbf{U}_p = \mathbf{U}_C + \mathbf{U}_D + \mathbf{U}_I + \mathbf{U}_T$  where  $\mathbf{U}_C$  = convective velocity,  $\mathbf{U}_D$  = diffusional velocity,  $\mathbf{U}_I$  = inertial velocity, and  $\mathbf{U}_T$  = thermophoretic velocity. An overview is given here. Convective velocity is given by the flow field. Diffusional, inertial and thermophoretic velocities are strong functions of the flowfield characteristics such as velocity gradients, concentration gradients and temperature gradients as well as local thermodynamic conditions.

The diffusional velocity is given as  $\mathbf{U}_D = -D_p^* (\nabla \ln(n^*))$  where  $D_p^*$  (the particle diffusion coefficient) is derived from kinetic theory as  $D_p^* = k_B T_f^* \tau^* / m_p$  [47].  $\tau^*$  is the particle relaxation time for particle motion due to the effects of the viscous drag force. For sub-critical Stokes number ( $Re_p < 1$ ),  $\tau^*$  is given by

$$\tau^* = \frac{\rho_p^* d_p^{*2} C_c}{18 \mu_f^*}$$

where  $C_c$  is the form of the Cunningham correction factor given in [45]. Inertial velocity is a modification of the form given by [49],  $\mathbf{U}_I = -\tau^* (\mathbf{U}_f^* \cdot \nabla) \mathbf{U}_f^*$ . The steady state conservation equations can be written as

$$\begin{aligned}
& (\mathbf{U}_p^* \cdot \nabla) \mathbf{U}_p^* + \frac{1}{\tau} (\mathbf{U}_p^* - \mathbf{U}_f^*) + \frac{1}{\rho_p^*} \nabla \cdot P_p^* = 0 \\
& \nabla \cdot (\rho_p^* \mathbf{U}_p^*) = 0
\end{aligned} \quad (10)$$

$$P_p^* \approx \frac{\mathbf{I}_p^* k T_p^*}{m_p^*}$$

where  $\tau$  is the relaxation time appearing the definition of the particle drag

$$\mathbf{F}_p^* = -\frac{m_p^*}{\tau} (\mathbf{U}_p^* - \mathbf{U}_f^*) \quad (11)$$



The current scheme assumes a relation first order in  $\tau$ , thus

$$\mathbf{U}_p = \mathbf{U}_f + \mathbf{U}_D + \mathbf{U}_I + \mathbf{U}_T \quad (12)$$

where

$$\mathbf{U}_I \approx (\mathbf{U}_f \cdot \nabla) \mathbf{U}_f \quad (13)$$

Several forms of the thermophoretic velocity have been given in the literature [47,48,50,45]. In general they can be written in the form  $\mathbf{U}_T^* = -K_T m_p \nabla T_f^* / \rho_p^*$  where  $K_T \equiv K_T(\mu_f^*, Kn_p)$  and  $Kn_p$  is the Knudsen number of the particle. For the present cases,  $K_T$  is assumed to be a linear function of  $\mu_f^*$  since it is generally a weak function of  $d_p^*$ , and  $\lambda^*$ . Using the following non-dimensionalization in conjunction with the non-dimensionalization used for fluid variables

$$M_k = \frac{M_k^*}{M_{k\infty}^*}, \quad r_p = \frac{r_p^*}{r_{p\infty}^*}, \quad v_p = \frac{v_p^*}{\frac{4}{3}\pi r_{p\infty}^3} \quad \text{and} \quad \rho_p = \frac{\rho_p^*}{\rho_{p\infty}^*} \quad (14)$$

the particle velocity in non-dimensional form is

$$\mathbf{U}_p = \mathbf{U}_f - \frac{1}{Sc Re_L} (\nabla \ln(n)) - St(\mathbf{U}_p \cdot \nabla) \mathbf{U}_p - \frac{K_T}{Re_L} \nabla T \quad (15)$$

where  $Re$  is the fluid Reynolds number

$$Re_L = \frac{\rho_p^* U_\infty L_\infty}{\mu_f^*}$$

$St$  is the Stokes number for sub critical  $Re$

$$St = \frac{\tau U_\infty}{L_\infty} = \frac{\rho_p d_p^2 C_c U_\infty}{18 \mu_f L_\infty}$$

and  $Sc$  is the Schmidt number

$$Sc = \frac{\mu_f^*}{\rho_p^* D_p^*} = \frac{\mu_f^* 18 \mu_f^* m_p^*}{\rho_p^* k_B T^* \rho_p^* d_p^{*2} C_c}$$

The Peclet number is defined as

$$Pe = Sc Re_L = \frac{U_\infty L_\infty}{D_p^*} = \frac{\mu_f^*}{\rho_p^* D_p^*} \frac{\rho_p^* U_\infty L_\infty}{\mu_f^*}$$

### 2.2.2. Aerosol dynamics

The general dynamic equation (GDE) including Brownian coagulation, condensation, evaporation, and nucleation is given by [50]

$$\begin{aligned} \frac{Dn_p^*}{Dt} + \frac{\partial(Gn_p^*)}{\partial v_p^*} - I_{Nuc}(v_p^0) \delta(v_p^* - v_p^0) \\ = \frac{1}{2} \int_0^{v_p^*} f_1(\beta, v_p^*, \tilde{v}_p^*, n_p^*, t^*) d\tilde{v}_p^* - n(v_p^*, t) \\ \times \int_0^{v_p^*} f_2(\beta, v_p^*, \tilde{v}_p^*, n_p^*, t^*) d\tilde{v}_p^* dv_p^* \end{aligned} \quad (16)$$

where the first term on the left is the total rate of change (substantive derivative) in number concentration including the non-convective transport terms, the second is the rate of change in number concentration due to condensation

at rate  $G$ , the third is the rate of formation of new particles of critical volume  $v_p^0$  at rate  $I_{Nuc}$ . The RHS represents the coagulation rate, where  $\beta$  is the collision frequency function. From classical nucleation theory [50], the nucleation rate for a given gas phase species ( $s$ ) is given by

$$I_{Nucs} = K_{Nucs} n_s^2 s_{1s} \left( \frac{k_B T_f^*}{2\pi m_{1s}} \right)^{\frac{1}{2}} S_s^2 \left( \frac{2}{9\pi} \right)^{\frac{1}{2}} \Sigma_s^{\frac{1}{2}} \exp \left( \frac{-k_s^0 \ln(S_s)}{2} \right) \quad (17)$$

$$\text{where } k_s^0 = \frac{\pi}{6} \left( \frac{4K_\Sigma S_s}{\ln(S_s)} \right)^3.$$

Since there is significant uncertainty in the prediction of nucleation rates, it is common to tune the classical rate to match data. Two methods are typically employed: a pre-multiplication factor for the entire nucleation term or an adjustment to the surface tension [51]. In the present work, the nucleation rate has been scaled by  $K_{Nuc}$  and surface tension is calculated based on a fourth order curve fit to experimental data.  $K_\Sigma$  is a parameter that adjusts for the ratio between the surface tension on a flat surface and that of a nucleating droplet.

### 2.2.3. Polydispersity modeling

There exist a number of methods to describe the behavior of polydisperse aerosols. The most general method assumes nothing about the aerosol distribution and models the general dynamic equation (GDE) using direct numerical simulation of individual particles. The computational expense of such simulations, however, means they are generally beyond the capabilities of current supercomputers, even for rudimentary problems and alternate methods must be used for practical applications. A typical approximation employed is the discrete sectional method [10] which sacrifices some accuracy in favor of computational efficiency. In this method, the size distribution is divided into a finite number of bins in which properties are averaged. The accuracy of the method is a function of the resolution of the particle size bins. Polydisperse aerosol behavior can be modeled more efficiently by making an assumption about the shape size distribution and solving the GDE in moment form for the properties of that distribution. This is the approach taken here.

It is assumed that the particle size distribution is lognormal, i.e.

$$n_p^*(v_p^*) = 1 / \left( 3\sqrt{2\pi} v_p^* \ln \sigma \right) \exp \left\{ -\ln^2(v_p^*/v_g^*) / 18 \ln^2 \sigma \right\} \quad (18)$$

where  $v_p^*$  and  $v_g^*$  are particle volume and geometric mean particle volumes, and is the geometric standard deviation of the size distribution. The lognormal distribution has the following properties:

$$\begin{aligned} v_p^{*k} &= v_g^{*k} \exp \left( \frac{9}{2} k^2 \ln^2 \sigma \right) \\ M_k^* &= M_o^* v_g^{*k} \exp \left( \frac{9}{2} k^2 \ln^2 \sigma \right) \end{aligned} \quad (19)$$

where  $M_k^* = \int_0^\infty v_p^{*k} n_p^*(v_p^*, t^*) dv_p^*$ .

In general, three equations are required to define the lognormal distribution. These can be obtained by multiplying the conservation equation by  $v_p^{*k}$  (where  $k$  is the moment of the size distribution) and integrating over all aerosol volumes to give the moment form of the particle conservation equation. We have chosen to solve for the zeroth, first and second moment conservation equations by setting  $k = 0, 1, 2$ . Other choices for the solved moments are possible. The geometric mean particle volume ( $v_g$ ) and the standard deviation of the distribution ( $\sigma$ ) can be defined from the zeroth, first and second moments as

$$v_g = \frac{M_1^2}{M_0^{1.5} M_2^{0.5}}, \quad \ln^2 \sigma = \frac{1}{9} \ln \left( \frac{M_0 M_2}{M_1^2} \right) + \ln^2 \sigma_\infty \quad (20)$$

where  $\sigma_\infty$  is the reference geometric mean standard deviation of the distribution [45].

In general,  $G$  and  $\beta$  take different forms for continuum, slip, and free molecular regimes [55,56]. One set of equations can be used for all regimes by using a harmonic average of the two equations for continuum and free molecular systems [29]. Substitution of  $U_p$  into the GDE yields a moment form representing three simultaneous partial differential equations. The properties of the distribution can be used to arrange the equations such that only the  $k$ th moment appears explicitly only in the  $k$ th moment equation [42], thus

$$\begin{aligned} & \rho \frac{\partial(M_k/\rho)}{\partial t} + \rho U_f \cdot \nabla(M_k/\rho) - \nabla \cdot \left( \frac{1}{Sc_k Re_L} \nabla M_k \right) \\ & + \nabla \cdot \left\{ M_k \left[ St_k (U_f \cdot \nabla) U_f + \frac{K_T}{Re_L T_f} \nabla T_f \right] \right\} \\ & = \gamma_k M_k^2 M_{k\infty} t_\infty \\ & + \sum_{s=1}^{N_s} \left( K_{\text{Cond}} \alpha_{ks} (S_s - 1) M_k + \frac{I_{\text{Nucs}}}{M_{k\infty}} (v_s^o)^k + \frac{I_{\text{RxnS}}}{M_{k\infty}} (v_{1s}^*)^k \right) t_\infty \end{aligned} \quad (21)$$

where  $k = 0, 1, 2$ . This resulting system of equations is strongly coupled both to each other and to properties of the flow (through  $Sc_k$ ,  $\gamma_k$ ,  $\alpha_k$ ,  $I_s$ ,  $T_f$ ,  $U_f$ ,  $C_s$  and  $S_s$ ).

The present model incorporates the factor  $K_{\text{Cond}}$  to adjust for the rate at which enthalpy of phase change can be conducted to the surrounding fluid. This is analogous to the condensation coefficient  $\alpha_c$  used by [8] and the Knudsen correction  $\phi$  used by [34] for the continuum regime. The polydisperse Stokes and Schmidt numbers ( $St_k$  and  $Sc_k$ ) can be written as

$$\begin{aligned} Sc_0 &= 1/(A_3 v_g^{-1/3} \exp(0.5 \ln^2 \sigma) + A_4 v_g^{-2/3} \exp(2 \ln^2 \sigma)) \\ Sc_1 &= 1/(A_3 v_g^{-1/3} \exp(-2.5 \ln^2 \sigma) + A_4 v_g^{-2/3} \exp(-4 \ln^2 \sigma)) \\ Sc_2 &= 1/(A_3 v_g^{-1/3} \exp(-5.5 \ln^2 \sigma) + A_4 v_g^{-2/3} \exp(-10 \ln^2 \sigma)) \end{aligned} \quad (22)$$

$$\begin{aligned} St_0 &= A_1 v_g^{2/3} \exp(2 \ln^2 \sigma) + A_2 v_g^{1/3} \exp(0.5 \ln^2 \sigma) \\ St_1 &= A_1 v_g^{2/3} \exp(8 \ln^2 \sigma) + A_2 v_g^{1/3} \exp(3.5 \ln^2 \sigma) \\ St_2 &= A_1 v_g^{2/3} \exp(14 \ln^2 \sigma) + A_2 v_g^{1/3} \exp(6.5 \ln^2 \sigma) \end{aligned} \quad (23)$$

and

$$\begin{aligned} A_1 &= \frac{2\rho^* U_\infty^*}{9\mu_f^* L_\infty} C^* r_{g\infty}^2, \quad A_2 = \frac{\rho_p^* U_\infty}{9\mu^* L_\infty} 3.314 \lambda^* r_{g\infty} \\ A_3 &= \frac{\rho_f^* k_B T_f^*}{6\pi\mu_f^{*2} r_{g\infty}} C^*, \quad A_4 = \frac{\rho_f^* k_B T_f^*}{12\pi\mu^{*2} r_{g\infty}^2} 3.314 \lambda^* \end{aligned} \quad (24)$$

Coagulation and condensation coefficients  $\gamma_k$  and  $\alpha_k$  are calculated from the harmonic average of the limiting cases for small (free molecular) and large (continuum) aerosols.

$$\begin{aligned} \gamma_0 &= \frac{\gamma_0^c \gamma_0^{\text{fm}}}{\gamma_0^c + \gamma_0^{\text{fm}}} \left( \frac{M_{0\infty} L_\infty}{U_\infty} \right), \quad \gamma_1 = 0, \\ \gamma_2 &= \frac{\gamma_2^c \gamma_2^{\text{fm}}}{\gamma_2^c + \gamma_2^{\text{fm}}} \left( \frac{M_{2\infty} L_\infty}{U_\infty} \right), \quad \alpha_{0s} = 0, \\ \alpha_{1s} &= \frac{\alpha_{1s}^c \alpha_{1s}^{\text{fm}}}{\alpha_{1s}^c + \alpha_{1s}^{\text{fm}}} \left( \frac{L_\infty}{U_\infty} \right), \quad \alpha_{2s} = \frac{\alpha_{2s}^c \alpha_{2s}^{\text{fm}}}{\alpha_{2s}^c + \alpha_{2s}^{\text{fm}}} \left( \frac{L_\infty}{U_\infty} \right) \end{aligned} \quad (25)$$

where

$$\begin{aligned} \gamma_0^c &= -B_4 \left[ 1 + \exp(\ln^2 \sigma) + B_5 Kn \exp \left( \frac{1}{2} \ln^2 \sigma \right) (1 + \exp(2 \ln^2 \sigma)) \right] \\ \gamma_0^{\text{fm}} &= -B_2 b_0 v_g^{1/6} \left[ \exp \left( \frac{25}{8} \ln^2 \sigma \right) + 2 \exp \left( \frac{5}{8} \ln^2 \sigma \right) + \exp \left( \frac{1}{8} \ln^2 \sigma \right) \right] \\ \gamma_2^c &= \frac{2B_4}{v_g^2} \exp(-27 \ln^2 \sigma) \left[ (1 + \exp(\ln^2 \sigma)) \right. \\ & \quad \left. + B_5 Kn \exp \left( -\frac{1}{2} \ln^2 \sigma \right) (1 + \exp(-2 \ln^2 \sigma)) \right] \\ \gamma_2^{\text{fm}} &= \frac{2B_2 b_2}{v_g^{11/6}} \exp(-36 \ln^2 \sigma) \left[ \exp \left( \frac{85}{8} \ln^2 \sigma \right) \right. \\ & \quad \left. + 2 \exp \left( \frac{89}{8} \ln^2 \sigma \right) + \exp \left( \frac{109}{8} \ln^2 \sigma \right) \right] \\ \alpha_{1s}^c &= B_{3s} v_g^{-2/3} \exp(-4 \ln^2 \sigma) \alpha_{1s}^{\text{fm}} = B_{1s} v_g^{-1/3} \exp \left( -\frac{5}{2} \ln^2 \sigma \right) \\ \alpha_{2s}^c &= B_{3s} v_g^{-2/3} \exp(-10 \ln^2 \sigma) \alpha_{2s}^{\text{fm}} = B_{1s} v_g^{-1/3} \exp \left( -\frac{11}{2} \ln^2 \sigma \right) \end{aligned} \quad (26)$$

The constants  $B_1$ ,  $B_2$ ,  $B_3$ ,  $B_4$  and  $B_5$  are related to thermodynamic properties of the system [29].  $b_o$  and  $b_2$  are given in [55].

### 2.3. Species conservation equations

For multi-species applications, the transport and consumption of individual species must be considered. In general, a separate continuity equation is required for each gas phase species. Thus for all species  $s$ , the saturation equation takes the form

$$\frac{\partial \rho C_s}{\partial t} + \nabla \cdot \left[ C_s \left( U_f - \frac{1}{Sc_s Re} \nabla (\ln C_s) \right) \right] = \Delta m_s \quad (27)$$

where  $C_s$  is the gas phase mass fraction for species  $s$ . The RHS represents the sources in mass due to nucleation, evaporation, condensation and chemical reaction.

## 2.4. Turbulence model equations

For turbulent calculations, a Reynolds averaged form of the flow, species and aerosol equations is used where the turbulent viscosity is calculated from a turbulence model from the Baldwin–Barth turbulence model. The resulting turbulent viscosity is then used to calculate the turbulent mass diffusivity in the aerosol moment and gas phase species equations as well as the total viscosity in the fluid equations. The Baldwin–Barth [52] one equation turbulence model is suitable for both internal and external flows.

$$\begin{aligned} \frac{\partial(v_l Re_t)}{\partial t} + \mathbf{U} \cdot \nabla(v_l Re_t) \\ = (c_{e2}f_2 - c_{e1})\sqrt{v_l Re_t \wp} + \left(v_l + 2\frac{v_t}{\sigma_\epsilon}\right)\nabla^2(v_l Re_t) \\ - \frac{1}{\sigma_\epsilon}(\nabla v_t) \cdot \nabla(v_l Re_t) \end{aligned} \quad (28)$$

where

$$\begin{aligned} \sigma_\epsilon &= \kappa^2/(c_{e2} - c_{e1})\sqrt{c_\mu} \\ v_t &= c_\mu(v_l Re_t)D_1D_2 \\ D_1 &= 1 - \exp(A_1^+/y^+) \\ D_2 &= 1 - \exp(A_2^+/y^+) \\ \wp &= v_l \left( \frac{\partial U_i}{\partial x_j} + \frac{\partial U_j}{\partial x_i} \right) \frac{\partial U_i}{\partial x_j} - \frac{2}{3}v_l \left( \frac{\partial U_k}{\partial x_k} \right)^2 \\ f_2 &= \frac{c_{e1}}{c_{e2}} + \left(1 - \frac{c_{e1}}{c_{e2}}\right) \left( \frac{1}{\kappa y^+} + D_1D_2 \right) \left( \sqrt{D_1D_2} + \frac{y^+}{\sqrt{D_1D_2}} \right) \\ &\quad \times \exp(A_1^+/y^+)D_2 + \frac{y^+}{\sqrt{D_1D_2}} \exp(A_1^+/y^+)D_2 \end{aligned}$$

### 2.4.1. Turbulent contribution to aerosol moment equations

The state of the art for turbulent modeling of particulates is weak, though several attempts at studying the effects have appeared in the literature. In general, it has been observed that particles in the micron and submicron range experience turbulent fluctuation of the same order of magnitude as the bulk fluid [53]. Larger particles do not experience a significant amount of turbulent fluctuation.

Reynolds' analogy between heat and mass transfer assumes  $D^t/\alpha^t = 1$  [54]. A similar analogy can be written for viscous and mass diffusivity, i.e.:  $0 < v^t/D^t < 1$  which can be written as a function of the particle Stokes number where here the turbulent flow eddy diffusivity is calculated using the Baldwin–Barth Turbulence model. The effects of the turbulent diffusivity are then added to the diffusion term via a correction factor to the viscosity.

$$\text{Turbulent Correction Factor} = 1 + \frac{\mu_t}{\mu_l} \left( \frac{D^t}{v^t} \right) \quad (29)$$

where  $\frac{D^t}{v^t} = f(St_k)$ . When Stokes number is large,  $f(St_k) \rightarrow 0$ . When Stokes number is small,  $f(St_k) \rightarrow 1$ . In this work, particles are in the submicron range and it is safe to assume

a small Stokes number as they are transported effectively with the turbulent eddies.

### 2.4.2. Coupling source terms

Gas and aerosol phases are indirectly coupled through thermodynamic parameters such as pressure and temperature, as well as directly influenced through source terms due to mass and energy transfer between the phases. Coupling source terms for mass and energy transfer between the bulk flow, individual gas phase species and aerosol moments are determined from the relevant system parameters via

$$\begin{aligned} \Delta m_s &= -\frac{I_{\text{Nucs}}k_s^0 + I_{\text{Rxn}}}{\tau_s} v_{1s} - \alpha_{1s}(S_s - F_s)M_1 + \sum_r \left( \frac{\partial C_s}{\partial t} \right)_r \\ \Delta m &= \sum_{s=1}^{N_s} \Delta m_s \\ \Delta H_t &= \sum_{s=1}^{N_s} \left( \left( -\frac{I_{\text{Nucs}}k_s^0}{\tau_s} v_{1s} - \alpha_{1s}(S_s - F_s)M_1 \right) dHV_s \right) \end{aligned} \quad (30)$$

where  $\Delta m$  and  $\Delta H_t$  appear in the bulk flow continuity and energy equations respectively and  $\Delta m_s$  appears in each species equation. The first term on the RHS represents the mass exchange due to nucleation and the second term represents the change due to condensation/evaporation.

### 2.4.3. Boundary conditions

The boundary conditions for the bulk flow are: no-slip at walls (pressure calculated) and  $P = \text{constant}$  at free surfaces (normal velocity calculated);  $H_t$  specified at the inflow and boundaries; inflow density and velocity are specified;  $P = \text{constant}$  at the inflow for supersonic inflows. Pressure alone is specified at the outflow for subsonic flows and  $\partial^2 P / \partial \xi^2 = 0$  for supersonic outflows. For subsonic inflow, a pressure and density are calculated based the characteristics of the Navier–Stokes equations via

$$\begin{aligned} P &= P_t / f^{+-} \left( \frac{\gamma}{\gamma-1} \right) \\ \rho &= \rho_t / f^{+-} \left( \frac{1}{\gamma-1} \right) \end{aligned} \quad (31)$$

where

$$\begin{aligned} C^+ &= 1 + 2/(\gamma - 1)a_\infty \\ C^- &= u_t + 2/(\gamma - 1)a \\ f^{+-} &= 1 + \frac{1}{2}(\gamma - 1) \left[ \frac{\frac{1}{2}(C^+ + C^-)}{\left[ \frac{(\gamma-1)}{4} (C^+ - C^-) \right]} \right]^2 \end{aligned} \quad (32)$$

Boundary conditions for the aerosols are;  $M_0$ ,  $M_1$  and  $M_2 = \text{constant}$  at the inflow,  $\partial M_k / \partial \eta = 0$ ,  $\partial M_k / \partial \xi = 0$  (slip or zero flux) or  $M_k = \text{constant}$  (non-slip) at the walls, and zero flux at free surfaces. The value of the constant can be used to reflect the nature of the boundary.  $M_k = 0$  reflects total capture of all particles that reach the wall.  $M_k$  between zero and unity reflects partial capture of particles.



Boundary conditions for the gas phase species are:  $C_s = \text{constant}$  at the inflow and  $\partial C_s / \partial \eta = 0$ ,  $\partial C_s / \partial \zeta = 0$  (zero flux) at the walls and free surfaces. Boundary conditions for the turbulent viscosity are:  $\nu R_t = \text{constant}$  at the inflow and free boundaries and  $\nu R_t = 0$  at the walls.

In all equations, for reversed flow at the downstream boundary, the flare approximation (in which streamwise convective terms are neglected) is used to eliminate downstream velocity, moment, species and turbulence boundary condition requirements. For 1-D and 2-D cases, appropriate cross-flow derivatives are dropped.

### 3. Discretization and solution procedure

Flow, species, turbulence and aerosol behavior are computed in separate modules using a finite difference discretization scheme and simultaneously marched in space based on the principles of the RNS methodology [43]. Details of the discretization of the governing equations and the local and global solution procedure are described below.

#### 3.1. Discretization

For all sets of equations, parabolic convective terms are upwind differenced with respect to the dominant flow direction ( $\xi$ ), and central differenced in the cross flow directions ( $\eta, \zeta$ ). Elliptic diffusion, heat flux and dissipation terms are central differenced in the cross flow directions and neglected in the streamwise direction. Additional terms that appear in the aerosol moment equations, i.e. thermophoretic and inertial terms are also treated according to their characteristics. Elliptic thermophoretic terms are neglected in the axial direction and central differenced in the cross plane. Parabolic inertial terms are upwind differenced in the axial direction and central differenced in the cross plane.

Since it is desired to determine the flow field in arbitrary geometries, and since it is necessary to resolve the solution in zones of high gradients, the finite difference representations of the governing equations are written in generalized three-dimensional non-orthogonal curvilinear coordinates and are solved in delta form to reduce the number of matrix inversions. In three dimensions the equations are discretized according to Table 1.

The equations are centered in the  $i$ -plane and staggered in the cross-plane ( $j, k$ -plane). Figs. 1 and 2 show the cross plane equation locations and grouping for internal and external flows. Note that the selection of variables associated with each equation is different than used in the traditional RNS methodology. In general, on solid walls, the normal momentum equation is used to calculate pressure and the normal velocity is prescribed. For free surfaces, the normal velocity is calculated and the pressure is prescribed.

For two-dimensional cases, the stencils reduce to three planes in the  $k$ -direction (Fig. 3). Boundary conditions on the  $k = 1$  and  $k = 3$  faces are slip conditions ( $\partial / \partial \zeta = 0$ ). The  $3 \times j_{\max}$  cross plane is then inverted as in the full three dimensional problem. For axisymmetric cases, the three planes are placed at an angle with a common vertex at  $j = 1$  and a small radius is added at the centerline to avoid a numerical singularity when  $r = 0$ .

#### 3.2. Global and local solution procedure

In the RNS methodology, axial diffusion terms are neglected, which allows an efficient spatial marching procedure in which only a single axial plane is treated implicitly. Coupling effects are calculated during the local solution procedure. Globally, a multi-sweep, space marching (global pressure relaxation) procedure is used in which the solution is marched in the approximate flow direction ( $\xi$  or  $i$ -direction). The full set of equations is converged at each  $\xi$  station before moving on to the next. Each  $i$ -plane is solved implicitly,  $i + 1$  and  $i - 1$  planes are treated explicitly and globally relaxed. Pressure is flux split in the streamwise direction according to the streamwise component of Mach number based on the parameter  $\omega = \min(M_\xi^2, 1)$  where  $M$  includes the particle contribution.

$$\frac{\partial p}{\partial \xi} = \omega_{i-1/2} \frac{(p_i - p_{i-1})}{(\xi_i - \xi_{i-1})} + \omega_{i+1/2} \frac{(p_{i+1} - p_i)}{(\xi_{i+1} - \xi_i)} \quad (33)$$

and

$$M_\xi = \frac{U_f}{a} = \frac{u_f \xi_x + v_f \xi_y + w_f \xi_z}{a(\xi_x^2 + \xi_y^2 + \xi_z^2)^{1/2}} \quad (34)$$

Table 1  
Equation differencing scheme

Equation	Equation location	Differencing		
		$i$ -direction	$j$ -direction	$k$ -direction
Continuity	$(i, j - 1/2, k - 1/2)$	Upwind	Trapezoidal	Trapezoidal
" $\xi$ " Momentum	$(i, j, k)$	Upwind	Central	Central
" $\eta$ " Momentum	$(i, j + 1/2, k)$	Upwind	Trapezoidal	Central
" $\zeta$ " Momentum	$(i, j, k + 1/2)$	Upwind	Central	Trapezoidal
Energy	$(i, j, k)$	Upwind	Central	Central
State	$(i, j, k)$	NA	NA	NA
Aerosol moments	$(i, j, k)$	Upwind	Central	Central
Gas phase species	$(i, j, k)$	Upwind	Central	Central
Turbulence model	$(i, j, k)$	Upwind	Central	Central

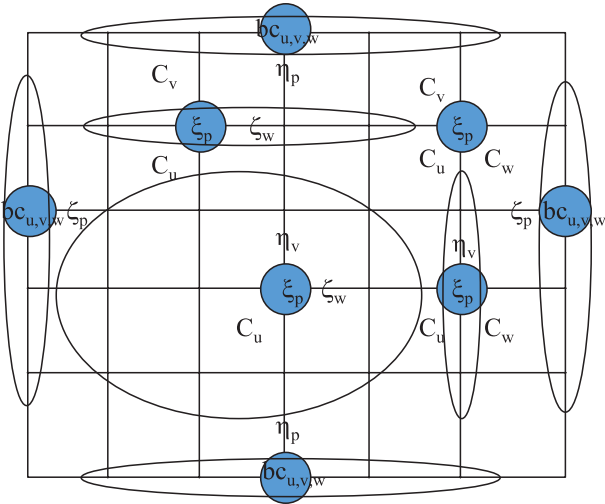


Fig. 1. Cross-plane ( $jk$ ) equation locations and groupings for 3-D internal flows. C = continuity,  $\xi = \xi$ -momentum,  $\eta = \eta$ -momentum,  $\zeta = \zeta$ -momentum, bc = boundary condition. Subscripts denote the unknown associated with each equation in coefficient matrix. Fluid state and energy equations as well as all moment and species equations are located at the grid points.

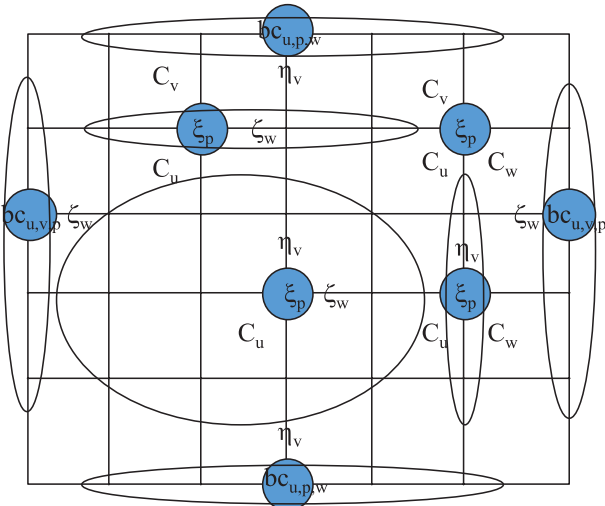


Fig. 2. Cross-plane ( $jk$ ) equation locations and groupings for 3-D internal flows. C = continuity,  $\xi = \xi$ -momentum,  $\eta = \eta$ -momentum,  $\zeta = \zeta$ -momentum, bc = boundary condition. Subscripts denote the unknown associated with each equation in coefficient matrix. Fluid state and energy equations as well as all moment and species equations are located at the grid point.

Streamwise convective terms in all the equations as well as inertial terms in the moment equations are upwind differenced based on the sign of  $U_r$ . In unseparated flow, upstream elliptic influences appear only through the pressure in the RNS equations (and, consequently, through the saturation ratio in the species and aerosol equations). Thus multiple sweeps are performed to carry the downstream pressure information forward. In reversed flow regions, all upwinded variables are relaxed in a similar manner since velocity at  $i+1$  must then be used in the  $i$ -plane calculations. For fully supersonic flows without

recirculation, the governing equations become parabolized and only a single global sweep is required to achieve convergence.

Coupling between the modules occurs during the local solution procedure. At every  $i$ -station, the sets of governing equations are solved sequentially. Each of these equations is nonlinear and thus must be iterated to convergence using Newton's method. Additionally, since flow, species, turbulence and aerosol equations (including local particle velocities) are also coupled to each other in a non-linear fashion, a second level of iteration is required.

In the RNS equations and species equations, the complete system is inverted at once. The three moment equations are solved in a semi-coupled fashion, in which the three equations are considered simultaneously with the coefficients on the coupling terms lagged one iteration. It has been found that this increases the stability over solving the equation simultaneously since the source terms in the moment equations due to nucleation, evaporation, condensation and coagulation can vary over many orders of magnitude. Increased stability is achieved at the expense of a slightly reduced rate of convergence.

### 3.3. Matrix inversion routines

The discretized fluid equations results in a block pentadiagonal coefficient matrix which is inverted using a sparse matrix solver. The discretized species, turbulence and aerosol moment equations result in a block tridiagonal coefficient matrix which is solved using a block tridiagonal solver. All four sets of difference equations are solved in delta form to reduce the number of inversions and thus the computational effort required to converge non-linear iterations. In delta form, the system of discretized non-linear equations

$$[A]\{x\}^{n+1} = (b)^n \quad (35)$$

can be written as

$$[A]\{\Delta x\}^{n+1} = (r)^n \quad (36)$$

where  $[A]$  is a square coefficient matrix,  $\{x\}^{n+1}$  is the solution vector,  $\{\Delta x\}^{n+1}$  is the change in solution vector in the delta-form,  $n$  is the iteration level and  $(r)^n = (b)^n - [A]\{x\}^n$  is the residual vector evaluated at the previous iteration. In this scheme, the residual goes to zero for the converged solution vector  $\{x\}$  for all coefficient matrices  $[A]$ . However, since both linear and nonlinear terms in the system of governing equations are treated implicitly, the elements of the coefficient matrix  $[A]$  depend on the solution, time-step, and grid related metrics terms, and thus the matrix needs to be inverted occasionally throughout the solution procedure to maintain effective convergence. Between matrix inversions, a computationally inexpensive back-substitution procedure is used using the previous LU decomposition for each system

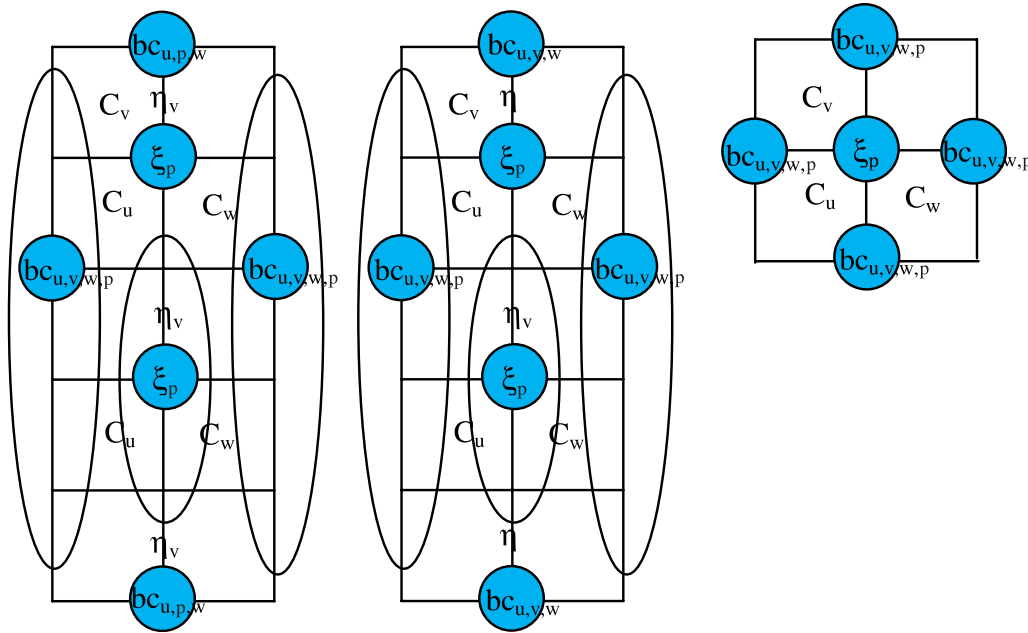


Fig. 3. Cross-plane ( $j, k$ ) equation locations and groupings for 2-D internal and external and quasi 1-D flows.  $C$  = continuity,  $\xi$  =  $\xi$ -momentum,  $\eta$  =  $\eta$ -momentum,  $\zeta$  =  $\zeta$ -momentum,  $bc$  = boundary condition. Subscripts denote the unknown associated with each equation in coefficient matrix. Fluid state and energy equations as well as all moment and species equations are located at the grid points.

of equations. Whenever the character of the solution changes during the marching procedure (due to a change in boundary conditions for instance), the matrix must be inverted once again.

#### 4. Code validation: comparison to limiting case solutions

A number of numerical simulations were carried out to validate the aerosol dynamics mechanisms in the model. These are chosen based on available limiting cases found in the literature for individual particle dynamics phenomenon important in strongly coupled gas particle flows. These include droplet coagulation, droplet condensation and evaporation, and combined nucleation, coagulation, and condensation. Finally, a validation case for a fully coupled case is presented. Validation of the bulk flow, turbulence, and particle transport equations have been carried out in our previous work [41,42] and are not revisited here. Relevant properties used in the following calculations are listed in Table 2. Grid convergence is here defined as a less than 1% change in the outflow variable values with a 50% increase in the number of grid points.

##### 4.1. Droplet coagulation in uniform flow

Comparisons with [55] and [56] for aerosol distribution properties for particles undergoing coagulation at finite times and as time approaches infinity were performed by running pseudo 1-D cases. Finite time conditions were achieved by setting a slip boundary condition at the wall, in a uniform flow and then setting  $U = 0.025$  m/s for various mean particle radii and initial standard deviations of

the particle size distribution. For uniform flow for 1 m, a residence time of 40 s is obtained. Initial particle size distributions of  $\sigma_\infty = 1$  and 2 were chosen with an inlet particle number concentration of  $1 \times 10^{15}$  #/m<sup>3</sup>. For all prescribed conditions,  $\sigma_g$  approaches the theoretical value of 1.355 for free-molecular limit and 1.32 for continuum limit as time approached infinity. Cases were run on a number of grids and grid convergence was reached with 101 axial grid points. Figs. 4 and 5 show comparisons to the results for finite time cases with the theoretical predictions. Agreement with the current model is excellent. Results show that larger standard deviations cause more rapid particle coagulation and thus more rapid increases in mean particle diameter.

##### 4.2. Water condensation and evaporations in uniform flow in the low concentration limit

Fig. 6 shows comparisons of the current method with the theoretical predictions of [47] for particle condensation and evaporation in uniform flow. Flow conditions are as in the previous coagulation cases. Initial particle concentrations are set to  $1 \times 10^5$  #/m<sup>3</sup> with initial standard deviations of the particle size distribution equal to unity. For condensation, the initial particle size is 10  $\mu$ m with a supersaturation of water vapor equal to 2.023 and for evaporation, the initial particle size is 20  $\mu$ m with a supersaturation of water vapor equal to 0 (dry air). Cases were run on a number of grids and grid convergence was reached with 61 axial grid points. Agreement between calculated and theoretical particle sizes is good, though the model slightly underpredicts condensation as compared to the theory.

Table 2  
Properties of gases and liquids used in calculations

Value	H <sub>2</sub> O	Air	CsOH	Units
MW		28.964	149.91	g/mol
$\gamma$	1.40	1.40	1.40	ND
$Pr$	1.00	0.71	0.71	ND
$\rho_p$	1000	N.A.	3675	kg/m <sup>3</sup>
$\Sigma = A + BT + CT^2 + DT^3$	$A = 0.05748778$ $B = 3.02908538 \times 10^{-4}$ $C = -1.0642578 \times 10^{-6}$ $D = 7.0700729 \times 10^{-10}$	NA	$A = 0.15286$ $B = -1.0660 \times 10^{-4}$ $C = 2.190 \times 10^{-8}$ $D = 0.00$	
$C_p = A + B/T^2 + C/T + DT + ET^2 + FT^3 + G/T^4 + H/T^5$	$A = 19.4174489$ $B = -228110.480$ $C = 3110.1366$ $D = 0.021859236$ $E = -1.522801 \times 10^{-06}$ $F = -1.73909 \times 10^{-09}$ $G = 4.9167 \times 10^{-13}$ $H = -3.89863 \times 10^{-17}$	$A = 25.84546229$ $B = 47860.76772$ $C = 0.00$ $D = 0.008900406$ $E = -2.34795 \times 10^{-6}$ $F = 2.1164 \times 10^{-10}$ $G = 0.00$ $H = 0.00$	$A = 50.92954195$ $B = -223544.1081$ $C = 0.00$ $D = 0.004977335$ $E = -5.82599 \times 10^{-7}$ $F = 0.00$ $G = 0.00$ $H = 0.00$	J/mol/K
$P_s$	$610.483 \left(\frac{273.2}{T}\right)^{5.1409} \times \text{Exp}(24.974 \frac{T-273.2}{T})$	NA	$101,325 \times \text{Exp}(2.3025809(\frac{-6750}{T} + 4.620))$	Pa
$\sigma$	2.641	3.711	5.06	m <sup>-10</sup>
$\varepsilon_k$	809.1	78.6	1129	K

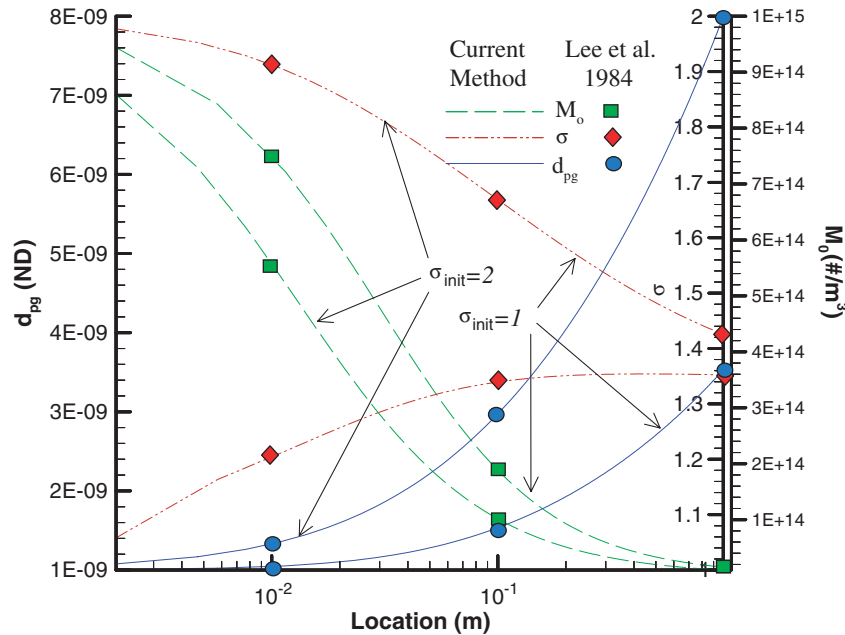


Fig. 4. Comparison of particle evolution in uniform flow due to coagulation in the free-molecular regime with the model of [55].

#### 4.3. CsOH nucleation, condensation and coagulation in the low concentration limit

To validate the particle nucleation and condensation terms and gas phase species coupling, comparisons are made with the sectional model of [23] in the one-way coupling limit, i.e. the particles are assumed not to affect the

gas properties, though the condensing species was conserved. Thus the fluid field was solved and the gas phase species and aerosols were solved using these frozen velocity and temperature fields. In this case, a mixture of CsOH vapor and air is introduced into a one-dimensional temperature field. Calculations were performed using the prescribed temperature field. All other parameters were

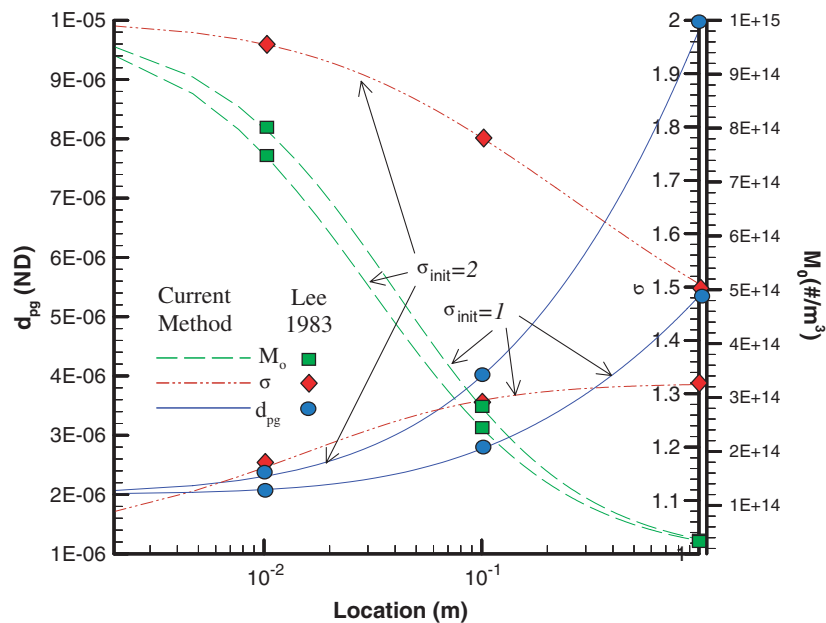


Fig. 5. Comparison of particle evolution in uniform flow due to coagulation in the free-molecular regime with the model of [56].

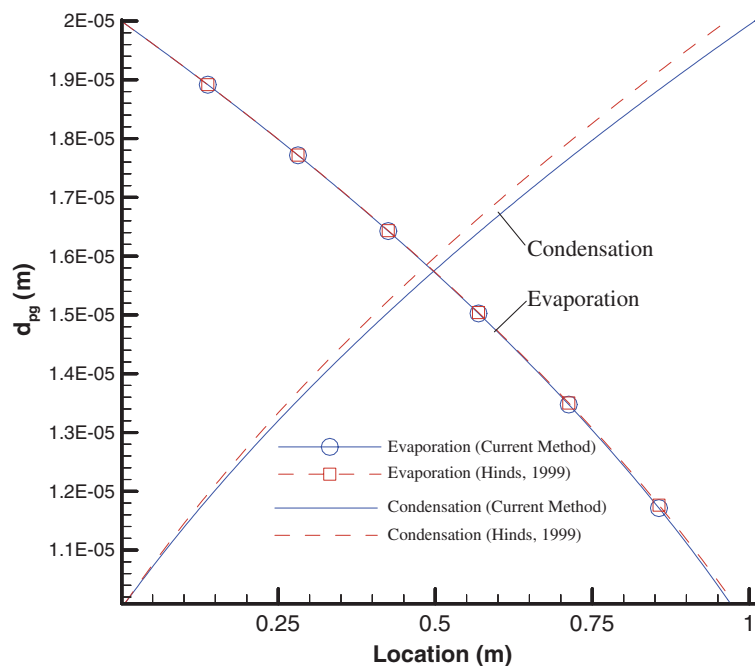


Fig. 6. Comparison of condensation and evaporation rates with the model of [47].

allowed to vary. Inlet conditions are  $T = 520^\circ\text{C}$  (793 K) ramping to  $480^\circ\text{C}$  (753 K) at  $x = .1\text{ m}$ ,  $U = 1\text{ m/s}$  and  $P = 1\text{ atm}$ . Inlet CsOH concentration is  $1\text{ g/N m}^3$ . This results in a CsOH mass fraction of  $8.4 \times 10^{-4}$ . The corrections of [34,17] were used in the calculation of the condensation and nucleation rates along with the properties in Table 3. The resulting number concentration of particles is low enough that coagulation is unimportant and so nucleation and condensation dynamics can be isolated.

Unlike the previous cases, due to the very low flow rate and high nucleation rate, gradients in particle properties are extremely sharp and the aerosol equations were found to require finer grids due to the high nucleation rates and resulting high gradients in the aerosol moments and a large number of grid points were needed to achieve grid convergence. This case was computed using a number of equally spaced grids ranging from 201 axial points. Grid convergence for the particle dynamic equations was reached at



Table 3

Comparison of the results for CsOH particle evolution in a temperature gradient to the model of [23]

	Current lognormal model (3 eqns)	Discrete sectional [23] (300 eqns)
$d_{pg}$ ( $\mu\text{m}$ )	0.147	0.147
$M_0$ ( $\#/\text{N m}^3$ )	$1.2 \times 10^{14}$	$1.2 \times 10^{14}$
$\sigma_g$	1.11	1.22
$S_{\text{CsOH}}$ (Peak)	3.25	3.26
% Condensed CsOH	71.9	71.8

3001 points. Resulting fluid and particle properties are shown in Fig. 7 as a function of axial location. The saturation ratio reaches a peak value of approximately 3.26, at which point large scale nucleation occurs and CsOH is rapidly converted from gas to condensed phase. The outflow value of the gas phase mass fraction was  $2.36 \times 10^{-4}$  kg/kg resulting in 71.9% conversion for CsOH vapor to the condensed phase. Comparisons with the sectional model of [23] using 300 particle size bins for the same conditions are shown in Table 3. The lognormal model and the sectional model were found to agree quite well as a significantly reduced computational cost, though the sectional method predicts a wider particle size distribution.

#### 4.4. Condensation shock formation in a two-dimensional wet steam nozzle

Validation of coupled flow and aerosol behavior requires simultaneous comparison of gas phase and aerosol phase parameters. Experiments that report both aerosol

and flow characteristics concurrently are scarce in the literature. Comparisons are made with the experimental results of [57] for condensing water aerosols in a de Laval nozzle using wet steam. In that work, pressure and  $d_{32}$  (Sauder mean) aerosol size were simultaneously measured along the centerline of the nozzle. Water vapor enters the nozzle subsonically and at a pressure below the saturation pressure. As the flow accelerates, pressure and temperature decrease, creating supersaturation conditions in a region downstream of the nozzle throat. Particles first form by homogeneous nucleation and then grow by condensation and coagulation. As mass is transferred from the gas phase to the liquid phase, heat is released forcing a “condensation shock” in the diverging section. The strength and location of the shock is directly related to the rates of mass and heat transfer due to nucleation and condensation, as well as indirectly due to changes in the aerosol properties due to the mass loading of droplets in the flow. These influences then couple back to the bulk flow which in turn alter the local thermodynamic conditions, the growth of the boundary layer, the gas expansion rate and the particle nucleation and growth rates.

The aerosol governing equations are solved in one-dimension and two-dimensions (inviscid and viscous/turbulent) under the conditions described in [57]. 1-D simulations were performed to assure  $\xi$ -grid independence. The axial grid was then used for 2-D calculations and  $\eta$ -grid independence studies were run. Grid converged solutions were achieved on a  $175 \times 45$  grid using symmetry conditions at the centerline. For these cases, the total pressure at the inlet is 25 Torr. The inlet Mach number corresponds

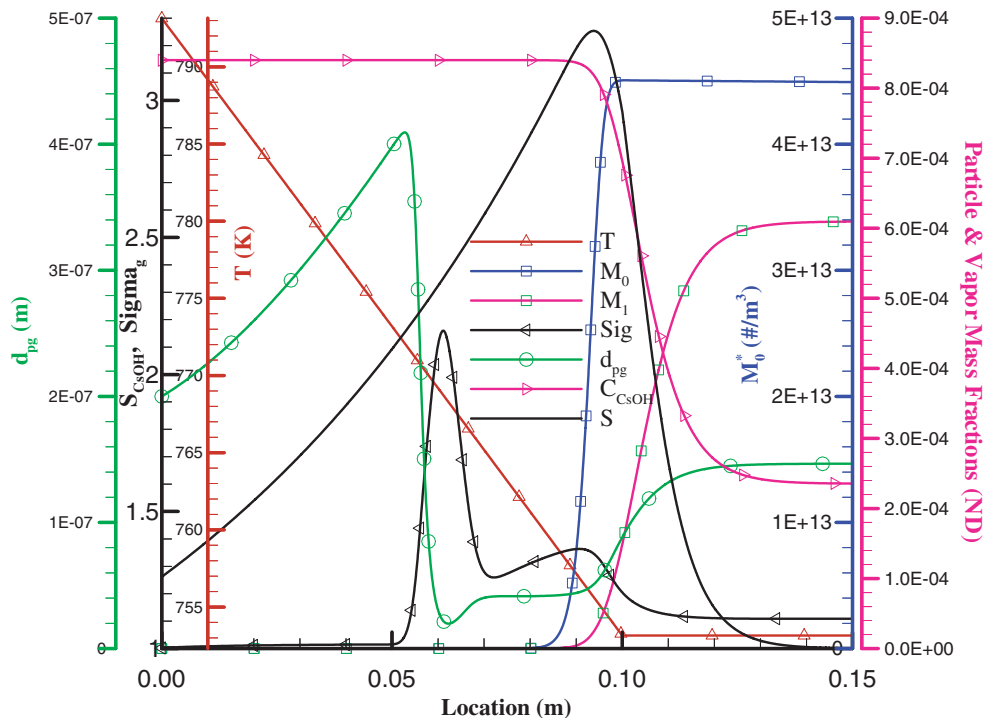


Fig. 7. Fluid, vapor and particle properties for CsOH droplet nucleation in a temperature gradient.

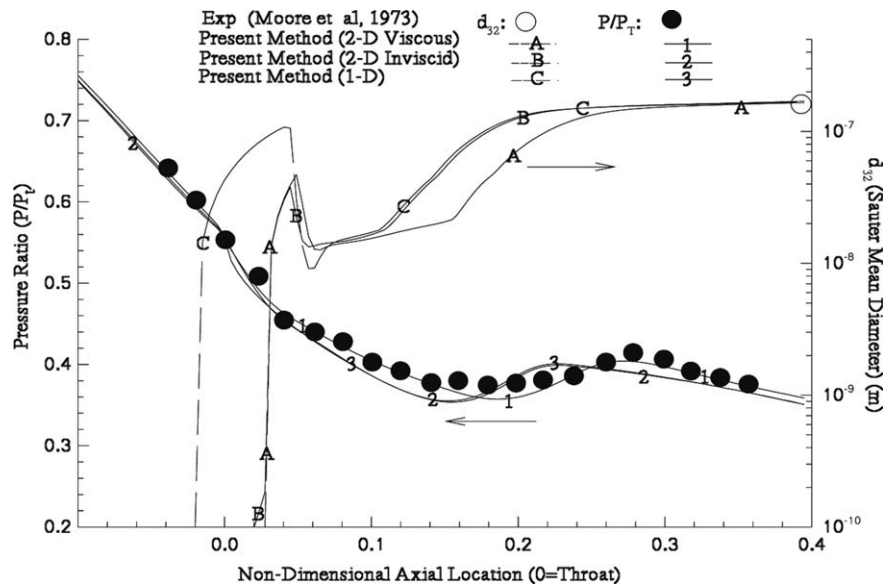


Fig. 8. Comparisons between the present 2-D viscous/turbulent, 2-D inviscid, and 1-D results with the experimental results of [57]. 2-D viscous/turbulent ( $P/P_t = \_1$ ;  $dg = \_A$ ), 2-D inviscid ( $P/P_t = \_2$ ;  $dg = \_B$ ), 1-D ( $P/P_t = \_3$ ;  $dg = \_C$ ).  $K_{Nuc} = 2.5 \times 10^3$ ,  $K_{Con} = 0.1$ ,  $K_\Sigma = 1.25$ .

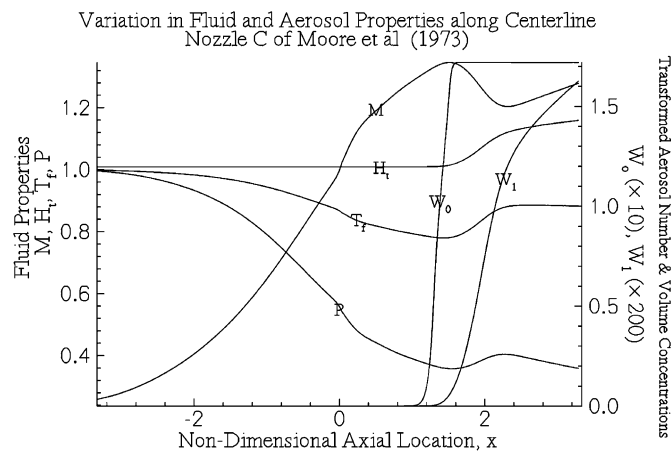


Fig. 9. Variation in non-dimensional fluid (Mach number ( $M$ ), total enthalpy ( $H_t$ ), temperature ( $T_t$ ) and pressure ( $P$ )) and aerosol properties (transformed aerosol number ( $W_0$ ) and volume ( $W_1$ ) concentrations) along the center line for [57] nozzle C (viscous/turbulent).

to choked flow at the throat based on isentropic conditions. This is valid since significant aerosol formation does not occur under the prescribed conditions until after the throat where Mach number is greater than unity and no significant upstream influence exists. The inlet temperature corresponds to 21 K below the temperature required for saturated dry steam for these conditions ( $T_{tr}^* = 359$  K). The Reynolds number, based on half channel height and inlet conditions, is  $2.06 \times 10^5$ . The resulting flow is turbulent. The condensation and nucleation rates and surface tension are adjusted based on the viscous/turbulent solution ( $K_{Nuc} = 2.5 \times 10^3$ ,  $K_{Con} = 0.1$ , and  $K_\Sigma = 1.25$ ).

As shown in Fig. 8, the results of the present model agree with data quite well for both gas phase and particle phase quantities. The condensation shock due to aerosol formation is captured in both strength and location, however, [57] only reported the  $d_{32}$  aerosol size at one

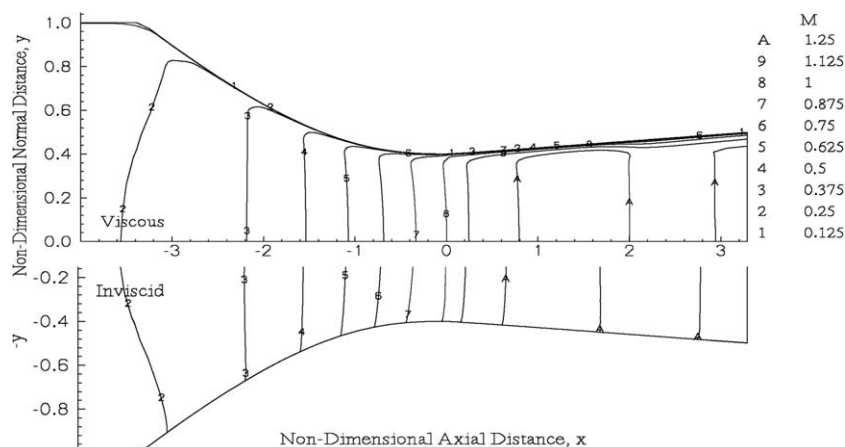


Fig. 10. Comparison of mixture Mach number ( $Ma$ ) for viscous/turbulent and inviscid cases for [57] nozzle C.

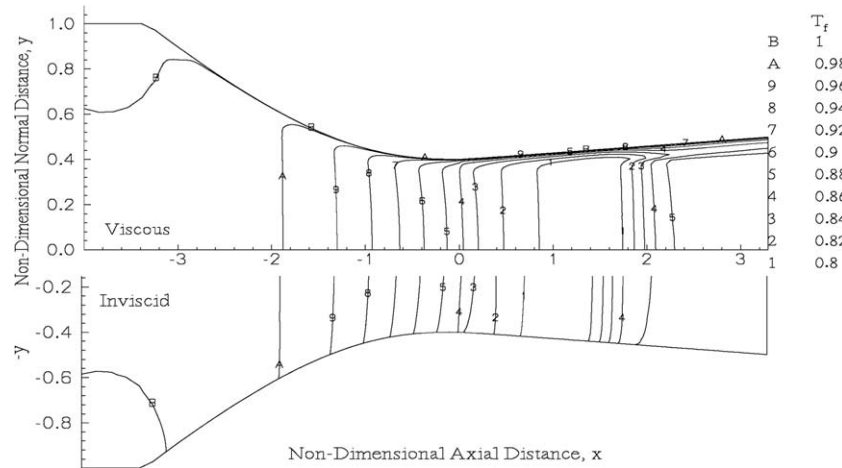


Fig. 11. Comparison of non-dimensional fluid temperature ( $T_f$ ) for viscous/turbulent and inviscid case for Moore et al. (3) nozzle C.

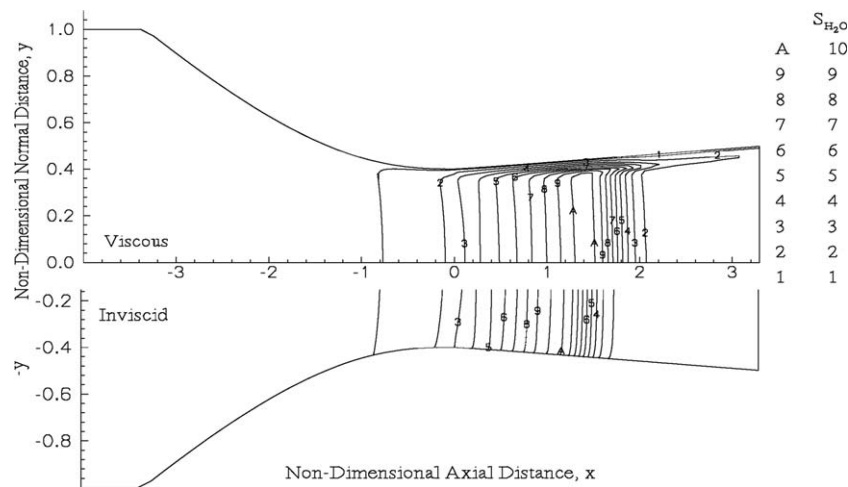


Fig. 12. Comparison of  $H_2O$  saturation ratios for viscous/turbulent and inviscid cases for Moore et al. (3) nozzle C.

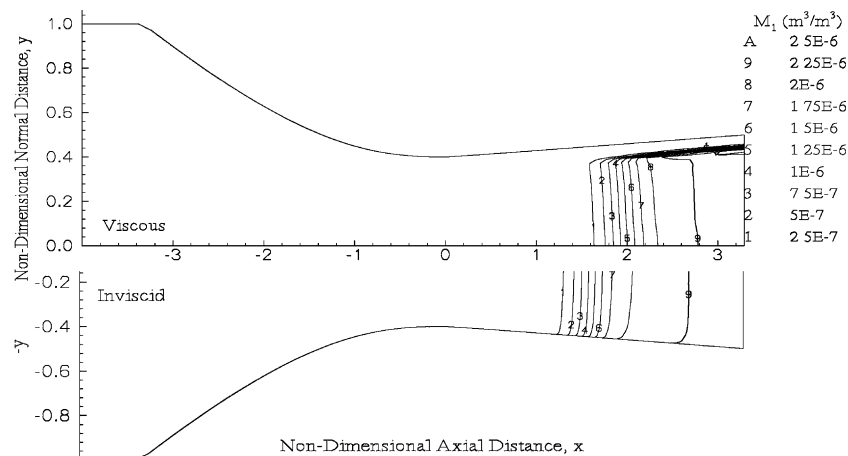


Fig. 13. Comparison of aerosol volume concentration ( $M_1$ ) for viscous/turbulent and inviscid cases for Moore et al. (3) nozzle C.

position. The case is also modeled using an inviscid wall (with slip boundary conditions on flow and aerosol quan-

ties) and in quasi-1-D. It can be seen that the effects of viscosity are very strong. Fig. 9 shows the centerline flow

and aerosol properties for the turbulent calculation. As particles form in the nozzle, energy is released into the gas phase causing enthalpy, temperature and pressure to rise. The aerosol formation process is eventually halted as the dropping pressure (due to expansion and scavenging of the gas phase) overcomes the effects of temperature, thus decreasing the saturation ratio below the critical level. However, with additional surface area available in the particle phase, a significant amount of mass and energy transfer continues to take place as particles grow by condensation. The viscous boundary layer (Fig. 10) slows the flow, and causes the temperature to rise to stagnation conditions at the wall (Fig. 11). The elevated temperature in the vicinity of the surface locally reduces the saturation ratio and suppresses aerosol formation (Fig. 12). This reduces the rate of heat and mass transfer between phases and changes the location of the condensation shock. The resulting aerosol volume concentration is shown in Fig. 13. Note the resulting low aerosol concentration near the wall for the viscous case as opposed to the high concentration in the inviscid case.

## 5. Conclusions

A moment model for polydisperse aerosol behavior incorporating the effects of nucleation, coagulation, evaporation, condensation, convection, diffusion, inertia and thermophoresis has been developed in general non-orthogonal coordinates and with the ability to capture strong mass and energy coupling between the gas and condensed phases in multi-dimensional flows. Limiting cases for particle evaporation and condensation and coagulation in the free molecular and continuum regimes have been modeled and validated against solutions in the literature. Combined nucleation/condensation dynamics have been modeled and validated against a sectional aerosol model for the dynamics in the low concentration limit where fluid particle coupling is one-way. The validated model has been successfully applied to water droplet formation in converging diverging nozzles with strong heat and mass transfer between the gas and particle phases and has been shown to be able to simulate both the polydispersity of the particle size distribution and mass and energy coupling effects between phases. Comparisons with experimental results for condensation shock formation in a two-dimensional wet steam nozzle show good agreement both in terms of the size of the droplets and the strength and location of the condensation shock. It has been demonstrated that the present moment model is useful in solving for the evolution of polydisperse aerosols in general flow applications. Aerosol properties such as the geometric mean particle size, mass and number concentrations, and the standard deviation of the particle size distribution can be efficiently calculated directly without having to sum up results for monodisperse aerosols over the entire particle spectrum and with a minimum computational effort. As these results indicate, the two-way coupling effects between aerosol behavior and

flow properties can be strong and multi-dimensional effects are found to be particularly important. Computational experiments reveal that the influence of viscous boundary layers are vital when predicting heat and mass transfer effects even in relatively high Reynolds number turbulent nozzle applications. This is due to the exponential dependency of the nucleation rate on the saturation ratio. This influence is found to be prominent even beyond the near wall viscous boundary layer region. The damping of nucleation significantly reduces the availability of surface area for heat and mass transfer by condensation and changes the overall expansion, nucleation and coagulation rates in the core of the flow as well as the strength and location of the condensation shock. Overall, these results indicate that an efficient moment based Eulerian approach combined with an economical RNS solution procedure allows the simultaneous resolution of important details of the bulk flow, the polydisperse particle properties and the interphase coupling effects in strongly coupled particle laden flows.

## Appendix A. Non-Dimensionalization

$$u = \frac{u^*}{U_\infty}, \quad x = \frac{x^*}{L_\infty}, \quad T = \frac{T^*}{T_\infty}, \quad \rho = \frac{\rho^*}{\rho_\infty}, \quad P = \frac{P^*}{\rho_\infty U_\infty^2}, \quad t = \frac{t^*}{\frac{L_\infty}{U_\infty}}, \quad t_\infty = \frac{L_\infty}{U_\infty}$$

$$M_k = \frac{M_k^*}{M_{k\infty}^*}, \quad r_p = \frac{r_p^*}{r_{p\infty}^*}, \quad v_p = \frac{v_p^*}{\frac{4}{3}\pi r_{p\infty}^*}, \quad \rho_p = \frac{\rho_p^*}{\rho_{p\infty}^*}$$

## Appendix B. Properties of the lognormal distribution

$$v_g = \frac{M_1^2}{M_0^{1.5} M_2^{0.5}} \quad (\text{N.1})$$

$$\ln^2 \sigma = \frac{1}{9} \ln \left( \frac{M_0 M_2}{M_1^2} \right) + \ln^2 \sigma_\infty \quad (\text{N.2})$$

$$M_k^* = \int_0^\infty v_p^{*k} n_p^{*k}(v_p^*, t^*) dv_p^* \quad (\text{N.3})$$

$$v_p^{*k} = v_g^{*k} \exp \left( \frac{9}{2} k^2 \ln^2 \sigma \right) \quad (\text{N.4})$$

$$M_k^* = M_0^{*k} v_g^{*k} \exp \left( \frac{9}{2} k^2 \ln^2 \sigma \right) \quad (\text{N.5})$$

## References

- [1] Smoluchowski V. Versuch einer Mathematischen Theorie der Koagulationskinetik Kollider Lösungen. Z Phys Chem 1917;92:129.
- [2] Kommu S, Khomami B, Biswas P. Simulation of aerosol dynamics and transport in chemically reacting particulate matter laden flows. Part I: Algorithm development and validation. Chem Eng Sci 2004; 59(2):345–58.
- [3] Kommu S, Khomami B, Biswas P. Simulation of aerosol dynamics and transport in chemically reacting particulate matter laden flows.

- Part II: Application to CVD reactors. *Chem Eng Sci* 2004;59(2): 359–371.
- [4] Leonard AD, Dai F. Applications of a coupled Monte Carlo PDF/finite volume CFD method for turbulent combustion. In: 30th AIAA/ASME/SAE/ASEE joint propulsion conference, AIAA-94-2904, 1994.
  - [5] Vikhansky A, Kraft M. Modelling of a RDC using a combined CFD-population balance approach. *Chem Eng Sci* 2004;59:2597–606.
  - [6] Lee BE, Tu JY, Fletcher CAJ. On numerical modeling of particle-wall impaction in relation to erosion prediction: Eulerian versus Lagrangian method. *Wear* 2001;252:168–79.
  - [7] Alhajraf S. Computational fluid dynamics modeling of drifting particles at porous fences. *Environ Model Software* 2004;19:163–70.
  - [8] Gerber AG, Kermani MJ. A pressure based Eulerian–Eulerian multiphase model for non-equilibrium condensation in transonic stream flow. *Int J Heat Mass Transfer* 2004;47:2217–31.
  - [9] Vicente W, Ochoa S, Aguilon J, Barrios E. An Eulerian model for the simulation of an entrained flow coal gasifier. *Appl Therm Eng* 2003;23(15):1993–2008.
  - [10] Gelbert F, Seinfeld JH. Simulation of multicomponent aerosol dynamics. *J Colloid Interf Sci* 1980;78:485–501.
  - [11] Wyslouzil BE, Wilemski G, Beals MG, Frish MB. Effect of carrier gas pressure on condensation in a supersonic nozzle. *Phys Fluids* 1994;6(8).
  - [12] Jokiniemi JK, Lazaridis M, Lehtinen KEJ, Kauppinen EI. Numerical simulation of vapour–aerosol dynamics in combustion processes. *J Aerosol Sci* 1993;25(3):429–46.
  - [13] Kwack X, Debenedetti PB. Mathematical modeling of aerosol formation by rapid expansion of supercritical solutions in a converging nozzle. *J Aerosol Sci* 1993;24(4):445–69.
  - [14] Xiong Y, Pratsinis SE. Gas phase production of particles in reactive turbulent flows. *J Aerosol Sci* 1993;22(5):637–55.
  - [15] Warren DR, Seinfeld JH. Simultaneous aerosol size distribution evolution in systems with simultaneous nucleation condensation and coagulation. *Aerosol Sci Technol* 1985;4:31–43.
  - [16] Forde M. Quasi-one-dimensional gas/particle flow with shock. *AIAA J* 1986;24(7):1196–9.
  - [17] Girshick SL, Chui CP, Muno R, Wu CY, Yang L, Singh SK, et al. Thermal plasma synthesis of ultrafine iron particles. *J Aerosol Sci* 1992;24(3):367–82.
  - [18] Wu CY, Biswas P. Study of numerical diffusion in a discrete-sectional model and its application to aerosol dynamic simulations. *Aerosol Sci Technol* 1998;29:359–78.
  - [19] Mathiesen V, Solberg T, Hjertager BH. Predictions of gas/particle flow with an Eulerian model including a realistic particle size distribution. *Powder Technol* 2000;112:34–45.
  - [20] White AJ, Young JB. Time marching method for the prediction of two-dimensional, unsteady flows of condensing steam. *J Propul Power* 1993;9(4):579–87.
  - [21] Muhlenweg H, Gutsch A, Schild A, Pratsinis SE. Process simulation of gas-to-particle-synthesis via population balances: investigation of three models. *Chem Eng Sci* 2002;57:2305–22.
  - [22] Johannessen T, Pratsinis SE, Livbjerg H. Computational analysis of coagulation and coalescence in the flame synthesis of titania particles. *Powder Technol* 2001;118:242–50.
  - [23] Pyykönen J, Jokiniemi J. Computational fluid dynamics based sectional aerosol modelling schemes. *J Aerosol Sci* 2000;31(5):531–50.
  - [24] Tsantilis S, Pratsinis SE, Haas V. Simulation of synthesis of palladium nanoparticles in a jet aerosol flow condenser. *J Aerosol Sci* 1998;30(6):785–803.
  - [25] Agterof WGM, Vaessen GEJ, Haagh GAAV, Klahn JK, Janssen JJM. Prediction of emulsion particle sizes using a computational fluid dynamics approach. *Colloids Surf B: Biointerf* 2003;31:141–8.
  - [26] Gidhagen L, Johansson C, Ström J, Kristensson A, Swietlicki E, Pirjola L, et al. Model simulation of ultrafine particles inside a road tunnel. *Atmos Environ* 2003;37:2023–36.
  - [27] Hulburt HM, Katz S. Some problems in particle technology. *Chem Eng Sci* 1964;19:555–67.
  - [28] Diemer RB, Olson JH. A moment methodology for coagulation and breakage problems: Part 2. Moment models and distribution reconstruction. *Chem Eng Sci* 2002;57:2211–28.
  - [29] Pratsinis S. Simultaneous nucleation condensation and coagulation in aerosol reactors. *J Colloid Interf Sci* 1988;124(2).
  - [30] Whitby E, Stratmann F, Wilck M. Merging and remapping modes in modal aerosol dynamics models: a “Dynamic Mode Manager”. *J Aerosol Sci* 2001;33:623–45.
  - [31] Megaridis CM, Dobbins RA. I bimodal integral solution of the dynamic equation for and aerosol undergoing simultaneous particle inception and coagulation. *Aerosol Sci Technol* 1990;12:240–55.
  - [32] McGraw R. Description of aerosol dynamics by the quadrature method of moments. *Aerosol Sci Technol* 1997;27:255–65.
  - [33] Brown DP, Biswas P, Rubin SG. Transport and deposition of particles in gas turbines: effects of convection, diffusion, thermophoresis, inertial impaction and coagulation. In: ASME FACT-vol. 18, Combustion Modeling, Scaling and Air Toxins; 1994.
  - [34] Brown DP, Rubin SG, Biswas P. Detailed modeling of gas-to-particle conversion in an axisymmetric nozzle using a coupled fluid/aerosol method. In: Sixth international symposium on computational fluid dynamics, vol. 1; 1995. p. 129–35.
  - [35] Wilck M, Stratmann F. A 2-D multicomponent modal aerosol model and its application to laminar flow reactors. *J Aerosol Sci* 1997;28(6): 959–72.
  - [36] Fan R, Marchisio DL, Fox RO. Application of the direct quadrature method of moments to polydisperse gas–solid fluidized beds. *Powder Technol* 2004;139:7–20.
  - [37] Moody E, Collins LR. Effect of mixing on the nucleation and growth of titania particles. *Aerosol Sci Technol* 2003;37:403–24.
  - [38] Jeong JJ, Choi M. Analysis of non-spherical polydisperse particle growth in a two-dimensional tubular reactor. *J Aerosol Sci* 2003;34: 713–32.
  - [39] Settumba N, Garrick SC. Direct numerical simulation of nanoparticle coagulation in a temporal mixing layer via a moment method. *J Aerosol Sci* 2003;34:149–67.
  - [40] Brown DP. Development and demonstration of a three-dimensional flow and aerosol model. In: AIAA 13th applied aerodynamics conference; 1995 June 19–22, Reno, Nevada.
  - [41] Brown DP. Efficient CFD model for polydisperse spray combustion. NIST SBIR 97-1-58, Final report, 1998.
  - [42] Brown DP. Development of a three-dimensional strongly coupled flow, species and aerosol model with applications to particle deposition, aerosol formation and pollution prediction 1996, Ph.D. Dissertation, University of Cincinnati.
  - [43] Rubin SG, Tannehill JC. Parabolized/reduced Navier–Stokes computational techniques. *Ann Rev Fluid Mech* 1992;24:117–44.
  - [44] Srinivasan K, Rubin SG. Solution based grid optimization through segmented domain decomposition. *J Comput Phys* 1997;136(2): 467–93.
  - [45] Bai H, Biswas P. Deposition of lognormally distributed aerosols accounting for simultaneous diffusion, thermophoresis and coagulation. *J Aerosol Sci* 1990;21(5):629–40.
  - [46] Heintzenberg J. Properties of the log-normal particle size distribution. *Aerosol Sci Technol* 1994;21:46–8.
  - [47] Hinds WC. Aerosol technology: properties, behavior and measurement of airborne particles. John Wiley & Sons; 1982.
  - [48] Talbot L, Cheng RK, Shefer RW, Willis DR. Thermophoresis of particles in a heated boundary layer. *J Fluid Mech* 1980;101(4): 737–58.
  - [49] de La Mora JF, Rosner DE. Effects of inertia on the diffusion of small particles to spheres and cylinders at low Reynolds numbers. *J Fluid Mech* 1982;125:379–95.
  - [50] Friedlander SK. Smoke, dust and haze. John Wiley & Sons; 1977.
  - [51] Hill PG. Condensation of water vapour during supersonic expansion in nozzles. *J Fluid Mech* 1965;25:593–620.
  - [52] Baldwin BS, Barth TJ. A one-equation turbulence transport model for high Reynolds number wall-bounded flows. NASA TM 102847, 1990.



- [53] Trichet P, Lavergne, G, Biscos Y. Amplitude and temporal response of droplets in a turbulent flow field. In: AIAA/ASME/SAE/ASEE joint propulsion conference, June, 1994, AIAA-94-3279.
- [54] White FM. Viscous fluid flow. McGraw-Hill Book; 1974.
- [55] Lee KW, Chen H. Coagulation of polydisperse particles. *Aerosol Sci Technol* 1983;3:327–34.
- [56] Lee KW, Chen H, Geiseke JA. Log-normally preserving size distribution for Brownian coagulation in the free-molecular regime. *Aerosol Sci Technol* 1984;3:53–62.
- [57] Moore MJ, Walters PT, Crane RI, Davidson BJ. Predicting the fog-drop size in wet-steam turbines. *Wet steam*, vol. 4. University of Warwick; 1973. p. 41–9.